

# Scene-based nonuniformity correction for focal plane arrays by the method of the inverse covariance form

Sergio N. Torres, Jorge E. Pezoa, and Majeed M. Hayat

What is to our knowledge a new scene-based algorithm for nonuniformity correction in infrared focal-plane array sensors has been developed. The technique is based on the inverse covariance form of the Kalman filter (KF), which has been reported previously and used in estimating the gain and bias of each detector in the array from scene data. The gain and the bias of each detector in the focal-plane array are assumed constant within a given sequence of frames, corresponding to a certain time and operational conditions, but they are allowed to randomly drift from one sequence to another following a discrete-time Gauss–Markov process. The inverse covariance form filter estimates the gain and the bias of each detector in the focal-plane array and optimally updates them as they drift in time. The estimation is performed with considerably higher computational efficiency than the equivalent KF. The ability of the algorithm in compensating for fixed-pattern noise in infrared imagery and in reducing the computational complexity is demonstrated by use of both simulated and real data. © 2003 Optical Society of America

*OCIS codes:* 100.2550, 040.1520, 110.3080, 100.3010, 100.3020.

## 1. Introduction

Focal-plane array (FPA) sensors are frequently used in a variety of visible and infrared imaging applications.<sup>1</sup> It is well known, however, that the performance of charge-coupled device infrared FPA sensors is seriously affected by the random spatial variation in the response of the array elements. The spatial nonuniformity in the array output, also referred to as fixed-pattern noise (FPN), is generally due to (1) the minute detector-to-detector variations in the optoelectronic characteristics of the detectors and (2) factors related to the array's readout circuitry and architecture. FPN is present even in the most advanced mid-wavelength and long-wavelength infrared sensors, and as one expects, it causes the broadening of the modulation transfer function and reduces the temperature-resolving capability of ther-

mal imaging systems.<sup>2</sup> Moreover, FPN can compromise the effectiveness of multi-sensor systems as it reduces the accuracy of the motion-estimation algorithms used by such systems. It is also known that FPN is not totally stationary but instead it varies slowly in time. Clearly, this drift in FPN makes a one-time laboratory calibration ineffective. Of course, one can calibrate frequently (e.g., by using a uniform black-body radiation source as a target), which would unfortunately require halting normal imaging operation during each calibration process.

In contrast to calibration-based nonuniformity correction (NUC), scene-based NUC is the process of FPN compensation by use of the very scenes or objects that are being imaged. However, the nondestructive nature of scene-based NUC comes at the expense of compromising radiometric accuracy, which may be required in certain applications such as spectral sensing but may be less critical in other applications such as thermal imaging. Scene-based NUC methods normally employ an image sequence and rely on motion (or changes in the actual scene) to provide diversity in the scene temperature per detector. This temperature diversity, in turn, provides a statistical reference point, common to all detectors, according to which the nonuniformity in the detectors' responses can be equalized.

To date, numerous scene-based NUC techniques have been reported in the literature.<sup>3–13</sup> Our group,

S. N. Torres and J. E. Pezoa are with the Department of Electrical Engineering, University of Concepción, Casilla 160-C, Concepción, Chile. Their e-mail addresses are storres@die.udec.cl and jpezoa@die.udec.cl. M. M. Hayat is with the Department of Electrical and Computer Engineering, University of New Mexico, Albuquerque, New Mexico 87131-1356. M. M. Hayat's e-mail is hayat@ece.unm.edu.

Received 20 January 2003; revised manuscript received 13 June 2003.

0003-6935/03/295872-10\$15.00/0

© 2003 Optical Society of America

in particular, has been active in the development of novel scene-based algorithms for NUC based on statistical estimation theory.<sup>14–17</sup> We have lately developed a Gauss–Markov dynamical model to capture the slow variation in the FPN and utilized the model to adaptively estimate the nonuniformity in the gain and bias by use of a Kalman filter (KF).<sup>16,17</sup> The input to the KF is taken as a sequence of fixed-length vectors of readout values representing a block of frames over which no significant drift occurs in the detectors’ gains and biases. As drift occurs and as a new vector of observations (block of frames) arrives, the KF updates the estimates of the gain and the bias of each detector. In this way, the valuable information contained in the old estimates is preserved and efficiently used in forming the current state of non-uniformity.

In this paper, we develop what is to our knowledge a new version of our earlier KF-based NUC technique<sup>17</sup> that is based on the inverse covariance form (ICF) of the KF. The ICF technique is computationally far more efficient than the original KF, especially when the dimension of the measurements is much greater than the dimension of the state vector (comprising the gain and bias). For example, in the ICF approach we require the inversion of a diagonal matrix with dimensions dictated by the length of the observation vector (e.g., >100) while in the original KF,<sup>17</sup> the inverse of a non-diagonal matrix of the same dimension is required. In addition to its superior computational efficiency, the ICF technique is better suited than its KF-based predecessor for situations where no reliable knowledge of the initial state of the gain and bias for each detector is available.<sup>18</sup>

This paper is organized as follows. In Section 2 the original KF-based NUC technique is reviewed. The ICF-based NUC technique is developed in Section 3. In Section 4 the ICF-based NUC technique is tested with sequences of infrared data with simulated nonuniformity and drift and its equivalence to the KF-based technique is empirically shown. In Section 5 the technique is applied to six sequences of real infrared data. The conclusions of the paper are summarized in Section 6.

## 2. Nonuniformity Model and the Kalman Filter

In this paper we adopt the linear-detector response assumption for which the detector output is approximately modeled with a temperature-independent gain and bias.<sup>16,17</sup> For a single detector in the FPA, vectors of readout data are considered corresponding to a series of blocks of frames for which no significant drift in the gain and the bias occurs within each block. For the  $k$ th block of frames, the linear input–output relation of the  $ij$ th detector in the  $n$ th frame is approximated by<sup>1,17</sup>

$$Y_k^{ij}(n) = A_k^{ij} T_k^{ij}(n) + B_k^{ij} + V_k^{ij}(n), \quad (1)$$

where  $A_k^{ij}$  and  $B_k^{ij}$  are the  $ij$ th detector’s gain and bias, respectively, at the  $k$ th block of frames.  $T_k^{ij}(n)$

represents the average number of photons that are detected by the  $ij$ th detector during the integration time associated with the  $n$ th frame of the  $k$ th block.  $V_k^{ij}(n)$  is the additive readout (temporal) noise associated to the  $ij$ th detector for the  $n$ th frame during the  $k$ th block of frames. In addition, the vector  $\mathbf{Y}_k^{ij} = [Y_k^{ij}(1) Y_k^{ij}(2) \dots Y_k^{ij}(l_k)]^T$  is an  $l_k$  dimensional vector of readout values for the  $ij$ th element of the FPA associated with the  $k$ th block. For simplicity of notation, the pixel superscripts  $ij$  will be omitted with the understanding that all operations are performed on a pixel-by-pixel basis.

According to the Gauss–Markov model that we introduced in our prior work,<sup>17</sup> we model the slow drift in the gain and the bias from one block of frames to another by

$$\begin{pmatrix} A_{k+1} \\ B_{k+1} \end{pmatrix} = \begin{bmatrix} \alpha_k & 0 \\ 0 & \beta_k \end{bmatrix} \begin{pmatrix} A_k \\ B_k \end{pmatrix} + \begin{bmatrix} 1 & 0 \\ 0 & 1 \end{bmatrix} \begin{pmatrix} W_k^{(1)} \\ W_k^{(2)} \end{pmatrix}, \quad (2)$$

which we can write compactly as

$$\mathbf{X}_{k+1} = \Phi_k \mathbf{X}_k + \mathbf{G}_k \mathbf{W}_k. \quad (3)$$

Here  $\mathbf{X}_k$  is the state vector comprising the gain  $A_k$  and the bias  $B_k$  at the  $k$ th block time and  $\Phi_k$  is the  $2 \times 2$  transition diagonal matrix between the states at  $k$  and  $k + 1$ , and its diagonal elements are the parameters  $\alpha_k$  and  $\beta_k$  representing the level of drift in the gain and bias, respectively, between consecutive blocks.  $\mathbf{G}_k$  is a  $2 \times 2$  noise identity matrix that randomly relates the driving (or process) noise vector  $\mathbf{W}_k$  to the state vector  $\mathbf{X}_k$ . The components of  $\mathbf{W}_k$  are  $W_k^{(1)}$  and  $W_k^{(2)}$ , the random driving noise for the gain and the bias, respectively, at the  $k$ th block time. A key requirement that we will impose on Eq. (2) is that the state vector must be a stationary random process because, in practice, drift in the gain and the bias randomly changes the FPN but it should not alter its severity. All others assumptions are shown and justified in detail elsewhere.<sup>17</sup>

The observation model for a given block of frames is an extension of the linear model (1) and it can be cast as

$$\begin{pmatrix} Y_k(1) \\ \vdots \\ Y_k(l_k) \end{pmatrix} = \begin{bmatrix} T_k(1) & 1 \\ \vdots & \vdots \\ T_k(l_k) & 1 \end{bmatrix} \begin{pmatrix} A_k \\ B_k \end{pmatrix} + \begin{pmatrix} V_k(1) \\ \vdots \\ V_k(l_k) \end{pmatrix} \quad (4)$$

or

$$\mathbf{Y}_k = \mathbf{H}_k \mathbf{X}_k + \mathbf{V}_k, \quad (5)$$

where  $\mathbf{H}_k$  is the observation matrix of dimension  $l_k \times 2$  and  $\mathbf{V}_k$  is the additive  $l_k$ -dimensional temporal noise vector. The main assumption in the observation model (4) is that the input  $T_k(n)$  in the  $k$ th block in any detector is an independent sequence of uniformly-distributed random variables in the range  $[T_k^{\min}, T_k^{\max}]$  common to all detectors in each block of frames.<sup>17</sup>

The KF-based NUC algorithm developed earlier<sup>17</sup> will be briefly visited here for completeness and com-

parison with the ICF technique. The algorithm is based on the following iterations<sup>17</sup>:

$$\hat{\mathbf{X}}_k^- = \Phi_{k-1} \hat{\mathbf{X}}_{k-1} + \mathbf{M}_{k-1}^T, \quad (6)$$

$$\mathbf{P}_k^- = \Phi_{k-1} \mathbf{P}_{k-1} \Phi_{k-1}^T + \mathbf{G}_{k-1} \mathbf{Q}_{k-1} \mathbf{G}_{k-1}^T, \quad (7)$$

$$\mathbf{K}_k = \mathbf{P}_k^- \bar{\mathbf{H}}_k^T [\bar{\mathbf{H}}_k \mathbf{P}_k^- \bar{\mathbf{H}}_k^T + \mathbf{S}_k]^{-1}, \quad (8)$$

$$\mathbf{S}_k = \mathbf{R}_k + \sigma_{T_k}^2 (\sigma_{A_0}^2 + \bar{A}_0) \mathbf{I}_{l_k, l_k}, \quad (9)$$

$$\hat{\mathbf{X}}_k = \hat{\mathbf{X}}_k^- + \mathbf{K}_k (\mathbf{Y}_k - \bar{\mathbf{H}}_k \hat{\mathbf{X}}_k^-), \quad (10)$$

$$\mathbf{P}_k = (\mathbf{I}_{2,2} - \mathbf{K}_k \bar{\mathbf{H}}_k) \mathbf{P}_k^-, \quad (11)$$

with the initial conditions

$$\hat{\mathbf{X}}_0 = E[\mathbf{X}_0] = \begin{pmatrix} \bar{A}_0 \\ \bar{B}_0 \end{pmatrix}, \quad \mathbf{P}_0 = \Lambda = \begin{bmatrix} \sigma_{A_0}^2 & 0 \\ 0 & \sigma_{B_0}^2 \end{bmatrix}. \quad (12)$$

In the above,  $\hat{\mathbf{X}}_k^-$  and  $\hat{\mathbf{X}}_k$  are respectively the *a priori* and the current state estimates,  $\mathbf{P}_k^-$  and  $\mathbf{P}_k$  are respectively the *a priori* and the current error covariance matrices, and  $\mathbf{K}_k$  is the Kalman gain matrix. The quantities  $\mathbf{Q}_k$  and  $\mathbf{R}_k$  are the auto and cross covariance functions of the driving noise and the additive noise, respectively,  $\bar{\mathbf{H}}_k$  is the mean of the observation matrix,  $\mathbf{M}_k$  is a vector containing the mean of the driver noise,<sup>16,17</sup>  $\sigma_{T_k}^2$  is the variance of the input infrared signal, and finally,  $\bar{A}_0$  ( $\bar{B}_0$ ) and  $\sigma_{A_0}^2$  ( $\sigma_{B_0}^2$ ) are the mean and variance of the initial condition for the gain (bias), respectively. The symbols  $\mathbf{I}_{2,2}$  and  $\mathbf{I}_{l_k, l_k}$  represent identity matrices of designated dimensions. Note that the matrices  $\mathbf{R}_k$  and  $\mathbf{S}_k$  are diagonal, square, and  $l_k$  dimensional. Also, note that Eqs. (6) and (7) are the KF updates, Eq. (8) yields the Kalman gain, and Eqs. (10) and (11) are the measurement updates.<sup>17</sup>

The foregoing Gauss–Markov model for the gain and bias is stable (i.e., it has bounded moments) since the drift parameters  $\alpha_k$  and  $\beta_k$  are taken to be strictly less than unity. Moreover, the estimation algorithm is also stable in that the error covariance matrix is convergent.<sup>18,19</sup> In our prior work, the convergence of the KF was tested with simulated data by showing that the error covariance matrix  $\mathbf{P}_k$  converges to a deterministic matrix.<sup>17,20</sup> Finally, according to our experience, we have never observed any instabilities when applying the algorithm to real infrared imagery.

With the above KF at hand, we proceed to develop the ICF of the filter.

### 3. Inverse Covariance Form of the Kalman Filter

The KF-based technique described in Section 2 normally estimates the nonuniformity parameters by use of a very large number of readout data. To accommodate such large data efficiently, the KF may be replaced by an equivalent ICF filter, which is an alternate form of the filter that produces the same state estimates but leads to substantial savings in computing operations and also provides improved numerical stability.<sup>18</sup> In this paper the ICF is derived follow-

ing the standard procedures given in Minkler and Minkler,<sup>18</sup> which consist of three main steps: (1) definition of the new equivalent state variables to be estimated, (2) application of the matrix inversion lemma to the Kalman-filter recursions to obtain the dual relationship for  $\hat{\mathbf{X}}_k$ ,  $\mathbf{P}_k$ ,  $\mathbf{K}_k$ ,  $\hat{\mathbf{X}}_k^-$ , and  $\mathbf{P}_k^-$ , and (3) determining the new initial conditions by use of the definition given in step 1.

#### A. Definition of the New Equivalent State Variables

The ICF is an alternative form of the KF for which the inverse of the error covariance matrix,  $\mathbf{P}_k^{-1}$ , is propagated in each iteration of the filter. Therefore, the ICF inherits the convergence properties of its equivalent KF. Following Minkler and Minkler,<sup>18</sup> the new equivalent variable to estimate,  $\hat{\mathbf{a}}_k$ , is defined as

$$\hat{\mathbf{a}}_k \triangleq \mathbf{P}_k^{-1} \hat{\mathbf{X}}_k, \quad (13)$$

where  $\hat{\mathbf{a}}_k$  is transmitted from one iteration of the filter to another instead of transmitting the error covariance matrix  $\mathbf{P}_k$  and the estimate  $\hat{\mathbf{X}}_k$ .

#### B. ICF Algorithm

We begin by recasting the first result of the matrix inversion lemma, which states that for any non-singular matrices  $\mathbf{L}$ ,  $\mathbf{M}$ , and  $\mathbf{N}$ ,  $(\mathbf{L} + \mathbf{M}\mathbf{N}^T)^{-1} = \mathbf{L}^{-1} - \mathbf{L}^{-1}\mathbf{M}(\mathbf{I} + \mathbf{N}^T\mathbf{L}^{-1}\mathbf{M})^{-1}\mathbf{N}^T\mathbf{L}^{-1}$ . We now apply this result to Eqs. (7), (8), and (11) to obtain expressions for  $(\mathbf{P}_k^-)^{-1}$  and  $\mathbf{P}_k^{-1}$  in terms of the system parameters  $\bar{\mathbf{H}}_k$ ,  $\mathbf{Q}_{k-1}$ ,  $\mathbf{S}_{k-1}$ , and  $\Phi_{k-1}$ .

Next, we invoke the second result of the matrix inversion lemma, which asserts that  $(\mathbf{L} + \mathbf{M}\mathbf{N}^T)^{-1}\mathbf{M} = \mathbf{L}^{-1}\mathbf{M}(\mathbf{I} + \mathbf{N}^T\mathbf{L}^{-1}\mathbf{M})$ . Now by applying this result and using the definition in (13), we can rewrite Eqs. (6) and (10) to get a recursive expression for  $\hat{\mathbf{a}}_k^-$  and  $\hat{\mathbf{a}}_k$  in terms of  $\hat{\mathbf{a}}_{k-1}$ . With the above calculations, the algorithm for the ICF of the KF is obtained and the recursions involved are listed below:

$$\hat{\mathbf{a}}_k = \{\mathbf{I}_{2,2} - \mathbf{D}_{k-1}\mathbf{G}_{k-1}^T\}\{\Phi_{k-1}^{-1}\hat{\mathbf{a}}_{k-1} + \mathbf{C}_{k-1}\mathbf{M}_{k-1}^T\}, \quad (14)$$

$$(\mathbf{P}_k^-)^{-1} = (\mathbf{I}_{2,2} - \mathbf{D}_{k-1}\mathbf{G}_{k-1}^T)\mathbf{C}_{k-1}, \quad (15)$$

$$\mathbf{C}_{k-1} \triangleq \Phi_{k-1}^{-T} \mathbf{P}_{k-1}^{-1} \Phi_{k-1}^{-1}, \quad (16)$$

$$\mathbf{D}_{k-1} \triangleq \mathbf{C}_{k-1} \mathbf{G}_{k-1} \{\mathbf{Q}_{k-1}^{-1} + \mathbf{G}_{k-1}^T \mathbf{C}_{k-1} \mathbf{G}_{k-1}\}^{-1}, \quad (17)$$

$$\hat{\mathbf{a}}_k = \hat{\mathbf{a}}_k^- + \bar{\mathbf{H}}_k^T \mathbf{S}_k^{-1} \mathbf{Y}_k, \quad (18)$$

$$\mathbf{P}_k^{-1} = (\mathbf{P}_k^-)^{-1} + \bar{\mathbf{H}}_k^T \mathbf{S}_k^{-1} \bar{\mathbf{H}}_k. \quad (19)$$

Equations (14) and (15) are the time updates of the ICF and the measurement update equations are given by Eqs. (18) and (19).

*Initial Conditions.* The initial conditions for the ICF of the filter can be derived by use of the definition in Eq. (13) as follows. In particular, we have

$$\mathbf{P}_0^{-1} \triangleq \Lambda^{-1}, \quad (20)$$

$$\bar{\mathbf{a}}_0 \triangleq \Lambda^{-1} \bar{\mathbf{X}}_0. \quad (21)$$

Table 1. Number of Operations (per Pixel and per Block of Frames)<sup>a</sup>

	Kalman Filter	Inverse Covariance Form
Additions	$l_k^2 + 3l_k^2p + l_k(2p^2 + p) + 3p^3 + p^2(m - 2) + p(m^2 + 2m - 1)$	$l_k^2(2p + 1) + l_k(p^2 - p + 1) + 4p^3 + p^2(4m - 1) + p(2m^2 - 3m - 1) + m^3$
Multiplications	$l_k^3 + 2l_k^2p + l_k(5p^2 + 4p) + 3p^3 + p^2(m + 2) + p(m^2 + m)$	$2l_k^2p + l_k(p^2 + p + 2) + 4p^3 + p^2(4m + 3) + 2pm^2 + m^3$

<sup>a</sup>Number that the Kalman filter and the inverse covariance form filter require for the  $k$ th iteration.  $p$  represents the dimension of the system state variables (which is 2 in our case) and  $l_k$  is the length of the observation vector.  $m$  represents the dimension of the random driving noise (also 2 in our case).

For estimation problems where no *a priori* knowledge of the initial system state is available, this algorithm is less susceptible to saturation problems within the equations, and in that sense, the algorithm may provide a numerically more stable approach.<sup>18</sup> In particular the ICF can be utilized with the initial condition  $\mathbf{P}_0^{-1} = \mathbf{0}$ , corresponding to an infinite  $\mathbf{P}_0$ . Note that in the traditional KF, this situation leads to saturation problems that consequently lead to significant (and possibly catastrophic) loss in numerical accuracy.

#### C. Comments on Computational Efficiency

We proceed to theoretically compare the number of operations per pixel and per block of frames between the ICF and the traditional KF assuming that the temporal readout noise and that the range of the input irradiance  $[T_k^{\max}, T_k^{\min}]$  are both common to all detectors on the FPA, but they may vary from block to block. Under the above assumptions, for each iteration  $k$ , the KF involves the inversion of the  $l_k \times l_k$  matrix  $[\mathbf{H}_k \mathbf{P}_k \mathbf{H}_k^T + \mathbf{S}_k]^{-1}$ . However, the ICF involves the inversion of the  $l_k$  dimension diagonal matrix  $[\mathbf{S}_k]^{-1}$ .

Table 1 shows the number of operations, per pixel and per block of frames at the  $k$ th iteration, required for the KF and the ICF. Note that for the KF, the relationship obtained between  $l_k$  and the number of operations is a third-order polynomial, while in the case of the ICF filter it is a second-order polynomial. Thus, a great reduction in computational load can be achieved. For example, with a block length of 500 frames, the KF needs 126,505,038 additions and 126,020,040 multiplications, while the ICF calculates 1,247,562 additions and 1,004,100 multiplications. Last, note that in Table 1 are detailed the nonstandard operations (in the context of a traditional KF with a deterministic observation matrix) that the NUC problem introduced in both the KF and the ICF filter.<sup>17</sup> (These refer to the operations in which the statistics of the random observation matrix  $\mathbf{H}$  are involved.)

#### 4. Applications to Simulated Infrared Data

In this Section the performance of the ICF filter is studied and compared with the performance of the traditional KF<sup>16,17</sup> by applying the algorithms to 8-bit infrared image sequences corrupted by simulated nonuniformity and drift. In all simulations, the gain and the bias are considered as mutually uncor-

related Gaussian random variables with mean values of unity and zero, respectively. Different levels of nonuniformity are introduced by varying the standard deviation of the gain and the bias. Different levels of drift in these parameters are also considered by modifying the inter-block correlation parameters  $\alpha_k$  and  $\beta_k$ . Temporal noise is simulated by use of a zero-mean Gaussian random variable that is uncorrelated to both gain and bias. The standard deviation of temporal noise is considered fixed at unity.<sup>11,14,15,17,21</sup> One hundred trials of each case were generated, and each trial included ten blocks, each containing 500 frames. NUC is performed by subtracting the estimated bias from the readout data and dividing the outcome by the estimated gain.

The performance of the ICF is evaluated by means of five metrics. To assess the estimation process, we compute the mean-square error (MSE) per block by averaging the square of the differences between the true and the estimated gain and bias over the entire array and all frames within each sequence. NUC capability is examined in terms of the root-mean-square error (RMSE), the correctability index,  $c$ , and the roughness parameter,  $\rho$ . The RMSE is defined as the square root of the average (over the entire array and block of frames) of the square of the difference between the true and the estimated collected photons in each pixel. The correctability parameter is computed with simulated flat-field data as the square root of the ratio between the FPN and the temporal readout noise.<sup>1,14,21</sup> The roughness parameter  $\rho$  is computed for any image  $f$  by use of<sup>14</sup>

$$\rho(f) \triangleq \frac{\|h_1 * f\|_1 + \|h_2 * f\|_1}{\|f\|_1}, \quad (22)$$

where  $h_1(i, j) = \delta_{i-1, j} - \delta_{i, j}$  and  $h_2(i, j) = \delta_{i, j-1} - \delta_{i, j}$ , respectively,  $\delta_{ij}$  is the Kronecker delta,  $\|f\|_1$  is the  $\ell^1$ -norm of  $f$ , and  $*$  represents discrete convolution. Note that  $\rho$  is zero for a uniform image, and it increases with the pixel-to-pixel variation in the image. Finally, an image-quality index that was recently introduced by Wang and Bovik<sup>22</sup> is modified and used here to further assess NUC capability. The proposed index is designed to regard any image distortion as a combination of two factors: luminance distortion and contrast distortion. Mathematically,



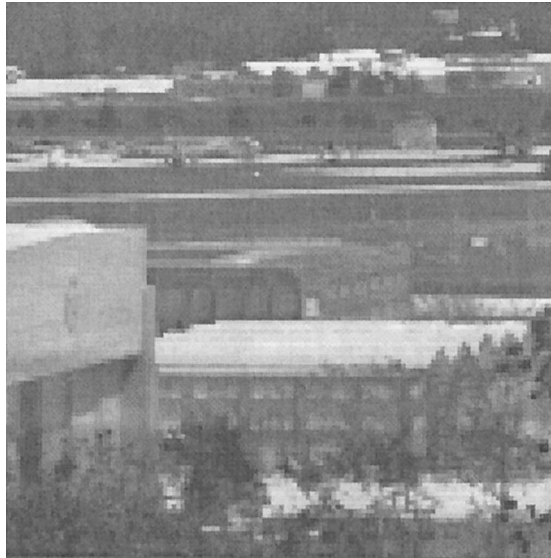


Fig. 1. Infrared imagery from the fifth block.

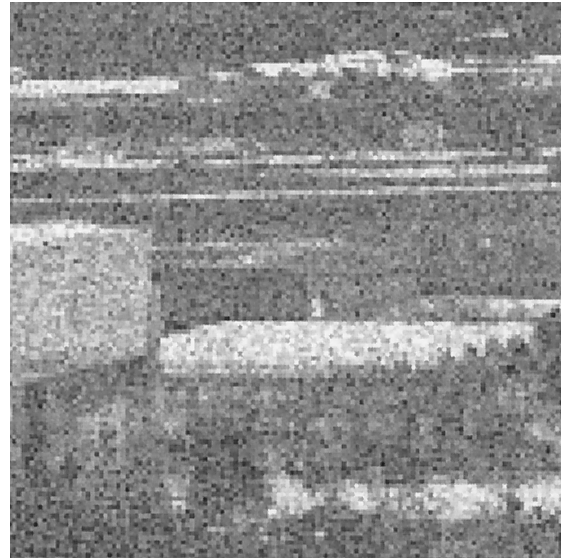


Fig. 2. Image of Fig. 1 corrupted with simulated nonuniformity generated with standard deviations of 0.10 and 10 for the gain and the bias, respectively.

the modified universal image quality index  $Q$  is defined by<sup>22</sup>

$$Q = \frac{4\bar{I}_1\bar{I}_2\sigma_{I_1}\sigma_{I_2}}{(\bar{I}_1^2 + \bar{I}_2^2)(\sigma_{I_1}^2 + \sigma_{I_2}^2)}, \quad (23)$$

where  $\bar{I}_1(\sigma_{I_1}^2)$  and  $\bar{I}_2(\sigma_{I_2}^2)$  are the spatial sample mean (spatial sample variance) of the true image and of the corrupted or compensated image, respectively. The dynamical range of the index  $Q$  is  $[-1, 1]$  with 1 representing the best performance.

#### A. Performance of the ICF and Its Numerical Equivalence to the Kalman Filter

In this Subsection the performance of the ICF filter in estimating the gain and the bias and its numerical equivalence to the KF are studied. We examined cases where the simulated nonuniformity and drift are added to blocks of both spatially-diverse and flat-field frames. The first case uses a collection of blocks of frames corrupted by simulated nonuniformity generated mainly by the gain. The bias nonuniformity was simulated by use of a Gaussian random variable with a fixed standard deviation of 10, while the standard deviation of the gain nonuniformity was varied from 1% to 20%. Low, moderate, and high levels of drift in the gain and the bias were considered by setting the correlation parameters  $\alpha_k = \beta_k$  to 0.95, 0.7, and 0.3, respectively. Figures 1 and 2 show a sample of a true infrared image and the corresponding artificially corrupted image (taken from the fifth block).

Consistent with our earlier work,<sup>17</sup> the empirical MSE in the estimated gain ( $MSE_A$ ) and bias ( $MSE_B$ ), the RMSE, the roughness parameter  $\rho$ , and the index  $Q$  are all independent of  $k$ . Table 2 shows the empirical performance parameters calculated for the fifth block ( $k = 5$ ) for low, moderate, and high levels of drift. The equivalence between the NUC capability of ICF and KF is clear from the performance met-

rics shown in the table. For example, both filters behave similarly in that the  $MSE_A$  and  $MSE_B$  decrease with the decrease in the drift.<sup>17</sup> However, note that the only discrepancy is found when high simulated drift is assumed ( $\alpha_k = \beta_k = 0.3$ ) and the error is attributable to numerical precision. In such a case, the  $MSE_B$  associated the ICF is eight times greater than that for the KF. However, it can be seen through the performance parameters RMSE,  $\rho$ , and  $Q$  that the quality of the NUC achieved is almost the same for both filters independently of the level of drift between the blocks of frames. Furthermore, examination of the index  $Q$  shows that the discrepancy between the compensated and the true frames is in both luminance and contrast. In particular, we observe an approximate loss of 13% in both the luminance and contrast in the corrected frames.

The dependence of the empirical MSE on the level of nonuniformity and drift is shown in Fig. 3. Note that when the standard deviation of the simulated gain nonuniformity is greater than 10%, the MSE increases with the increase in the level of nonuniformity. However, Fig. 4 shows that such MSE increase is not reflected in the image quality parameters  $Q$  and  $\rho$ , nor is it detected by the naked eye. Figures 5 and 6 depict the corrected versions of the image in Fig. 2 obtained by the KF and ICF, respectively.

Similar results were obtained when the FPN was generated primarily by the bias. For brevity, we only comment on parts of the results. The parameters RMSE and  $\rho$ , computed for the corrected and raw sequences of frames (with a medium drift), reveal a reduction in the nonuniformity by 48% and 51%, respectively for each parameter; whereas, the  $Q$  index increases by 39%.

Last, we applied the ICF and the KF filters to blocks of 500 frames of noisy flat-field data. Various

Table 2. Performance Parameters MSE, RMSE,  $\rho$ , and  $Q$  at the  $k = 5$  block<sup>a</sup>

$\alpha_k = \beta_k = 0.95$			$\alpha_k = \beta_k = 0.70$			$\alpha_k = \beta_k = 0.30$		
Parameter	ICF	KF	Parameter	ICF	KF	Parameter	ICF	KF
RMSE <sub>u</sub>	0.173	0.173	RMSE <sub>u</sub>	0.244	0.244	RMSE <sub>u</sub>	0.301	0.301
RMSE <sub>c</sub>	0.147	0.147	RMSE <sub>c</sub>	0.147	0.149	RMSE <sub>c</sub>	0.153	0.149
MSE <sub>A</sub>	0.021	0.021	MSE <sub>A</sub>	0.024	0.024	MSE <sub>A</sub>	0.027	0.024
MSE <sub>B</sub>	1.055	0.999	MSE <sub>B</sub>	1.630	0.999	MSE <sub>B</sub>	8.824	0.999
$\rho_u$	0.317	0.317	$\rho_u$	0.317	0.317	$\rho_u$	0.318	0.318
$\rho_c$	0.180	0.180	$\rho_c$	0.180	0.180	$\rho_c$	0.182	0.180
$Q_u$	0.649	0.649	$Q_u$	0.651	0.651	$Q_u$	0.651	0.651
$Q_c$	0.878	0.878	$Q_c$	0.876	0.876	$Q_c$	0.873	0.874

<sup>a</sup>As a function of the simulated level of drift between blocks. The subscripts u and c indicate whether the parameters were computed for the uncorrected and the corrected blocks, respectively. The nonuniformity is generated with standard deviations for the gain and the bias of 0.10 and 5, respectively.

levels of temporal noise were considered, and each block of frames contained different levels of amplitudes in the gray-scale range of 60–240.<sup>17</sup> The results indicated that the correctability in the corrected block is approximately unity for both the ICF and the KF. In fact, we have found that the so-called temporal-noise threshold, which is the standard deviation of the temporal noise that yields a unity correctability parameter, is 0.75, which is a number valid for blocks of frames represented in the specified gray-scale range.<sup>17,21</sup>

#### B. Dependence on the Initial Condition

To evaluate the sensitivity of the ICF filter on inaccuracies in the initial condition of the error covariance matrix  $\mathbf{P}_0$ , simulated nonuniformity was added to a sequence of blocks of infrared data and initial conditions in which varying errors were considered. Specifically, the diagonal elements of  $\mathbf{P}_0$  were as-

sumed  $10^6$ , 1, and  $10^{-3}$ , representing high, medium, and small errors, respectively. It was observed that with block lengths greater than 500 frames, and regardless of the level of nonuniformity and drift, no tangible change was observed in the MSE, RMSE,  $\rho$ , and the  $Q$  index as the initial condition was varied. For example, using the same simulation parameters as in Subsection 4.A (e.g., a standard deviation in the gain nonuniformity equivalent to 20% of the mean gain under a high-drift condition), we found that  $\rho$  and  $Q$  were respectively 0.190 and 0.856 for the large initial error and 0.120 and 0.843 for the small initial error.

Moreover, we found that the MSE computed using the parameters estimated by the KF exhibits a small increase (approximately 10%) with the increase in the initial error from  $\mathbf{P}_0 = 10^{-3}$  to  $\mathbf{P}_0 = 10^6$ . However, such increase in the MSE is almost not seen on the corrected frames by the RMSE,  $\rho$ ,  $Q$ , and the naked eye.

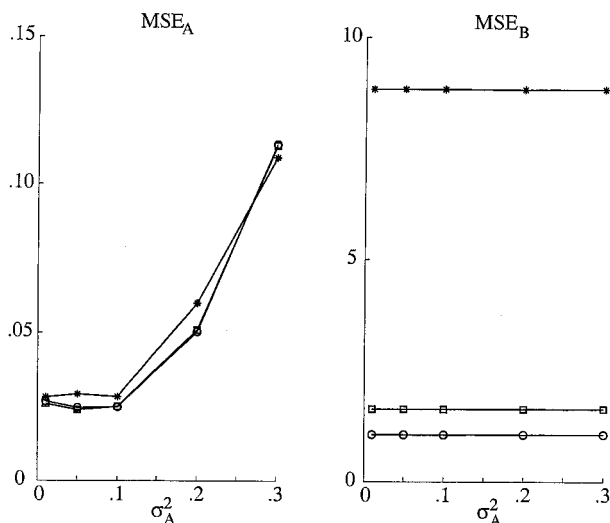


Fig. 3. MSE of the gain and the bias as a function of the level of nonuniformity generated mainly by the gain. The standard deviation for the bias is 5 (relative to an 8-bit scale). Open circles represent low drift ( $\alpha_k = \beta_k = 0.95$ ), open squares represent moderate drift ( $\alpha_k = \beta_k = 0.7$ ), and the asterisks represent high drift ( $\alpha_k = \beta_k = 0.3$ ).

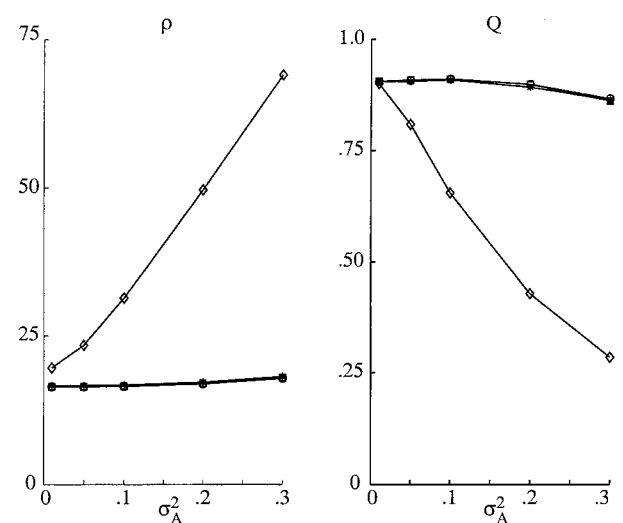


Fig. 4. Roughness parameter,  $\rho$ , and the  $Q$  index as a function of the level of gain-dominated nonuniformity. The bias standard deviation is fixed at 5. Open circles represent low drift ( $\alpha_k = \beta_k = 0.95$ ), open squares represent moderate drift ( $\alpha_k = \beta_k = 0.7$ ), and the asterisks represent high drift ( $\alpha_k = \beta_k = 0.3$ ). Open diamonds represent the corresponding parameters for the uncorrected block.

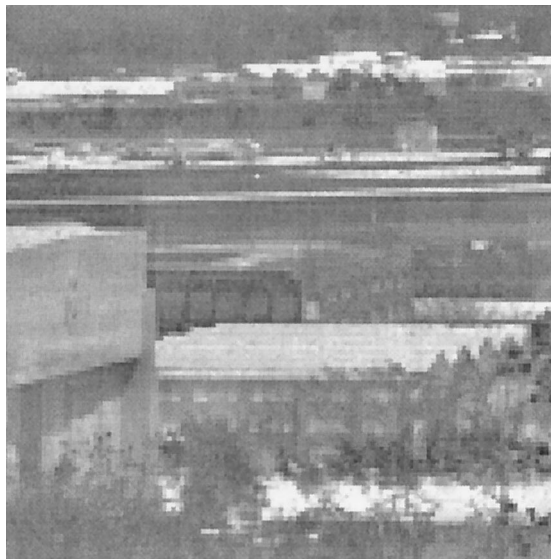


Fig. 5. Frame of Fig. 1 corrected by use of the traditional KF.

### C. Computational Efficiency

A theoretical estimate of the CPU time employed by both versions of the filter can be obtained if we conveniently assume, for instance, that a floating-point addition takes a unit of time and the floating-point multiplication takes two units of time.<sup>23</sup> In real computer systems, however, memory hierarchy, operating system planning, and many other practical factors must be taken into account and a theoretical evaluation is not enough. Figure 7 shows the actual CPU time consumed by the KF and the ICF filters versus the block length. Reductions of 55% in time is obtained for block lengths in excess of 1000 frames. These tests were made with a Pentium IV (1.6 GHz) processor and a 768-MB RAM in conjunction with Matlab's cputime function.

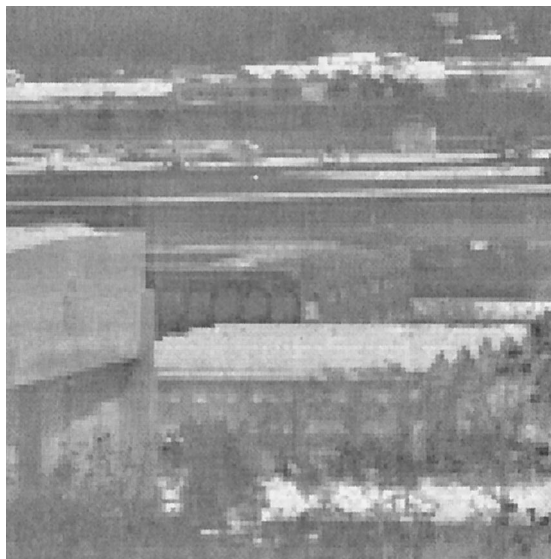


Fig. 6. Frame of Fig. 1 corrected by use of the ICF Filter.

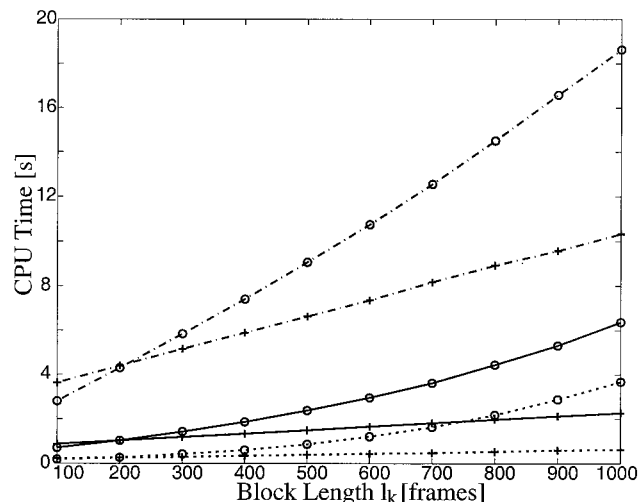


Fig. 7. CPU time consumed by the traditional KF and the ICF filter as a function of the block index  $k$ . Open circles and crosses represent the CPU time consumed by the traditional Kalman and the ICF filters, respectively. The dotted curve represents a frame size of  $32 \times 32$  pixels, the solid curve represents the case of  $64 \times 64$  pixels, and the dashed-dotted curve represents the case of  $128 \times 128$  pixels.

### 5. Applications to Real Data

In this section the ICF algorithm is applied to six blocks of terrestrial mid-wave infrared (3–5  $\mu\text{m}$ ) imagery that were collected with a  $128 \times 128$  InSb FPA cooled camera (Amber Model AE-4128). Five blocks of imagery were collected at different hours of the same day (6:30 AM, 8 AM, 9:30 AM, 11 AM, and 1 PM), and each block originally contained 4200 frames captured at a rate of 30 frames per second (fps). The sixth set of data, collected much earlier in the day, contains 1200 frames. The blocks will be labeled as  $k = 1, \dots, 6$ , corresponding to 6:30 AM, 8 AM, 9:30 AM, 11 AM, 1 PM, and the last block, respectively.

Owing to the fact that the camera readout output was quantized to 16-bit integers, we conveniently took the range of the average infrared photon numbers collected by each detector as  $[T_k^{\min}, T_k^{\max}] = [0, 2^{16} - 1]$ , where  $k = 1, \dots, 6$ . In addition, the initial inverse of the error covariance matrix  $\mathbf{P}_0^{-1}$  is selected to be near zero (which implies severe inaccuracy in the assumed initial condition). The initial state vector  $\mathbf{X}_0$  was selected within the practical range (16-bit representation) for the gain and the bias values for the above infrared FPA camera.<sup>17</sup> Moreover, the following set of initial conditions (common to all detectors) were assumed for the gain and bias:  $A_0 = 1.0$ ,  $B_0 = 0$ ,  $\sigma_{A_0}^2 = 0.1$  and  $\sigma_{B_0}^2 = 5000$ . These values were chosen heuristically as follows: Unity and zero mean values for the gain and the bias, respectively, were chosen to maintain the dynamical range of the output. On the other hand, the initial standard deviations of the gain and bias were arbitrarily chosen within 10% of the assumed mean values. Last, because the true drift in the gain and the bias are unknown, the ICF filter was repeatedly ap-



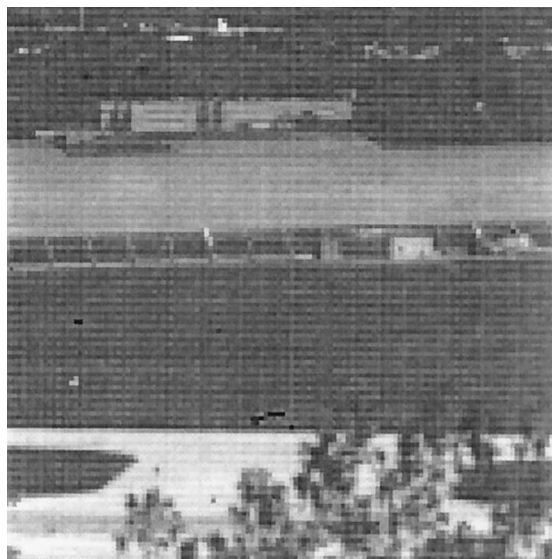


Fig. 8. Infrared imagery from block 5.

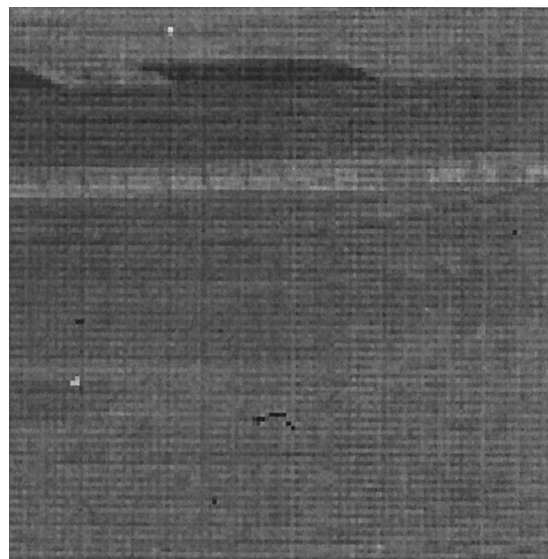


Fig. 10. Imagery from the first block (corresponding to 6:30 AM).

plied while the drift parameters  $\alpha$  and  $\beta$  were allowed to vary from 0.05 to 0.95 in steps of 0.15.

Throughout the calculations, we limited the number of frames used in the algorithm to only 500 consecutive frames per block (i.e.,  $l_k = 500, k = 1, \dots, 6$ ). The tests performed demonstrated that for  $\alpha_k = \beta_k = 0.95$ , which represents a weak drift between the blocks, a very good NUC was achieved for blocks 2 through 5. For example, Figs. 8 and 9 show a raw frame and the corresponding corrected frame for the block at  $k = 5$ . Note that the ICF filter also compensates for the dead pixels that appears in the raw imagery, as they are interpreted by the algorithm as cases of extremely low gain. The computed mean of  $\rho$  shows a reduction in the nonuniformity of 58% at  $k = 2$ , 39% at  $k = 3$ , 36% at  $k = 4$ , and 19% at  $k = 5$ .

The sequence in the first block (corresponding to 6:30 AM) contains less diversity in the collected irradiance than the blocks at  $k = 2, \dots, 5$ . The motion was limited in the first block, and the irradiance range was also limited as most of the objects in the scenes were cold. Figures 10 and 11 show the raw frame and the corresponding ICF corrected frame, respectively. Note that the quality of the compensation is much poorer than the one obtained in the fifth block (corresponding to 1 PM). This poor performance is partially due to the fact that in the calculation of the gain and bias in the first block, no past knowledge of these parameters is being used. Now, Fig. 12 depicts the corrected version of the frame in Fig. 10 when the block at 6:30 is moved from  $k = 1$  to  $k = 5$ . The improvement in the correction is due to the fact that the ICF filter

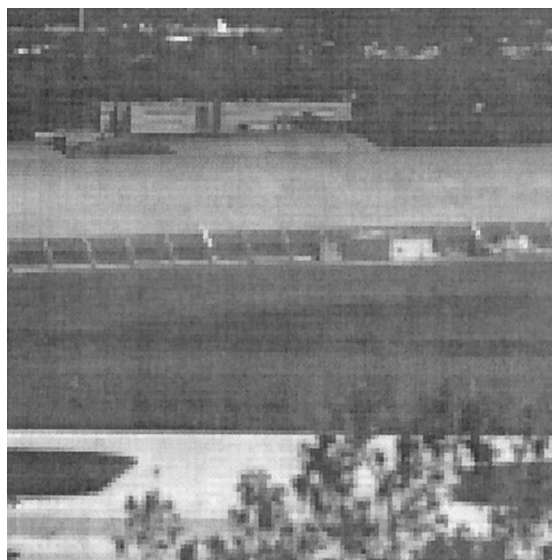


Fig. 9. Frame of Fig. 8 corrected by use of 500 consecutive frames per block with the drift factors taken as  $\alpha_5 = \beta_5 = 0.95$ .



Fig. 11. Frame of Fig. 10 corrected by use of 500 consecutive frames per block and correlation factors  $\alpha_1 = \beta_1 = 0.95$ .



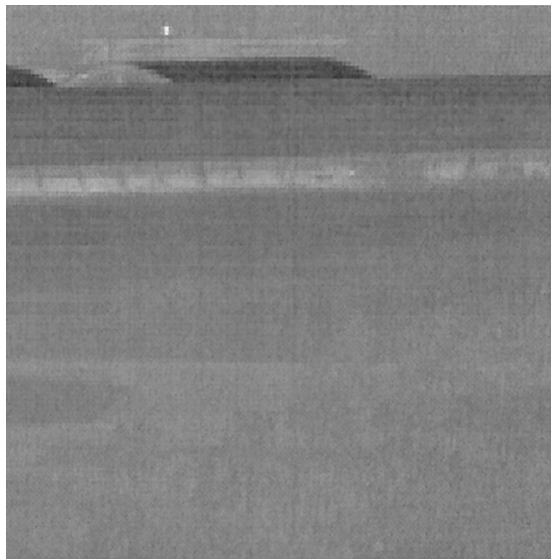


Fig. 12. Frame of Fig. 10 corrected by use of 500 consecutive frames per block, for which we stipulate that the first block arrives after the fourth block (in place of the existing fifth block). The drift factors are taken as  $\alpha_5 = \beta_5 = 0.95$ .

now uses the information gained in the previous blocks (first block through fourth block) for estimating the gain and the bias for  $k = 5$ .

Finally, the sixth block was captured before sunrise and only one target (a jet aircraft) is seen. Correction obtained for the sixth block was somewhat satisfactory, but ghosting artifacts appeared over the corrected images. Ghosting occurs because most of the objects in the fifth block are not present in the sixth block, and moreover, the sixth block is poor in motion and also lacks spatial diversity in the infrared scenes. For example, Figs. 13 and 14 depict the raw frame and its correction, respectively. The ghosting artifacts can be seen as shadows around the target. We have observed that such ghosting artifacts can be

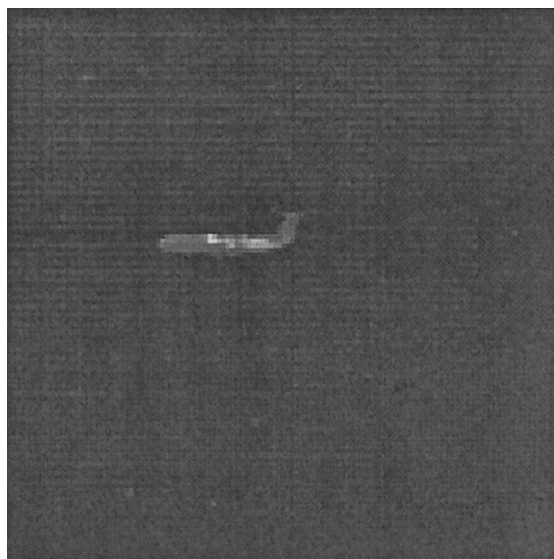


Fig. 13. Imagery from the sixth block.



Fig. 14. Frame of Fig. 13 corrected by use of 500 consecutive frames per block and correlation factors  $\alpha_6 = \beta_6 = 0.95$ .



Fig. 15. Frame of Fig. 13 corrected by use of 800 consecutive frames per block and correlation factors  $\alpha_6 = \beta_6 = 0.8$ .

reduced using more frames and assuming higher levels of drift between the blocks. Figure 15 shows the corrected version of Fig. 13 by use of more frames and higher drift than the correction shown in Fig. 14.

Last, the drift in the estimated gain and the bias between blocks 2 and 3, 3 and 4, and 4 and 5 are respectively found to be 5%, 0.5%, and 10% for the gain and 40%, 27%, and 29% for the bias. This shows that the drift in the gain is smaller than the drift in the bias, which is consistent with the two-point calibration results performed earlier.<sup>16,17</sup>

## 6. Conclusions

In this paper we used the inverse covariance form to develop an equivalent but computationally efficient

version of the previously reported Kalman filter technique for nonuniformity correction in FPAs. Moreover, our simulations and real data evaluations have tested practically that the ICF of the KF is better suited for problems where no reliable estimate of the initial condition is available. This feature is in accord with the theoretically expected robustness of the ICF to erroneous initial conditions.<sup>18</sup> The theoretical evaluation demonstrates that the number of floating-point additions and multiplications per pixel and per block of frames in every iteration is a function of the block length  $l_k$ . For the original Kalman filter, the relationship obtained between  $l_k$  and the number of operations is a third-order polynomial while in the case of the inverse covariance form filter it is a second-order polynomial. Empirical results have shown that the CPU time consumed by the inverse covariance filter is considerably less than the CPU time employed by the Kalman filter, and that time is independent of the frame size. For example, for a block length of 1000 frames reductions of 45%, 41%, and 50% in the CPU time were obtained for frame sizes of  $128 \times 128$ ,  $64 \times 64$ , and  $32 \times 32$  pixels, respectively. The performance of the inverse-covariance-form version of the Kalman filter is demonstrated by use of simulated and real infrared imagery showing the ability of the technique in updating the estimates of the gain and bias nonuniformity as new data arrives. Possible extensions of the technique include developing an adaptive method for the estimation of the drift parameters from blocks of infrared scene data.

This work was supported by the Fondo Nacional de Ciencia y Tecnología of the Chilean Government, project number 1020433, and the National Science Foundation. The authors thank Ernest E. Armstrong (OptiMetrics Inc.) for collecting the data, and the United States Air Force Research Laboratory, Ohio.

## References

1. G. C. Holst, *CCD Arrays, Cameras and Displays* (SPIE Optical Engineering Press, Bellingham, Wash., 1996).
2. P. Tribolet, P. Chorier, A. Manissadjian, P. Costa, and J. P. Chatard, "High performance infrared detectors at Sofradir," in *Infrared Detectors and Focal Plane Arrays VI*, E. L. Dereniak and R. E. Sampson, eds., Proc. SPIE **4028**, 438–456 (2002).
3. P. M. Narendra and N. A. Foss, "Shutterless fixed pattern noise correction for infrared imaging arrays," in *Technical Issues in Focal Plane Development*, W. S. Chan and E. Krikorian, eds., Proc. SPIE **282**, 44–51 (1981).
4. P. M. Narendra, "Reference-free nonuniformity compensation for IR imaging arrays," in *Smart Sensors II*, D. F. Barbe, ed., Proc. SPIE **252**, 10–17 (1980).
5. J. G. Harris, "Continuous-time calibration of VLSI sensors for gain and offset variations," in *Smart Focal Plane Arrays and Focal Plane Array Testing*, M. Wigdor and M. A. Massie, eds., Proc. SPIE **2474**, 23–33 (1995).
6. J. G. Harris and Y.-M. Chiang, "Nonuniformity correction using constant average statistics constraint: analog and digital implementations," in *Infrared Technology and Applications XXIII*, B. F. Andersen and M. Strojnik, eds., Proc. SPIE **3061**, 895–905 (1997).
7. J. G. Harris and Y.-M. Chiang, "Minimizing the 'ghosting' artifact in scene-based nonuniformity correction," in *Infrared Imaging Systems: Design, Analysis, Modeling, and Testing IX*, G. C. Holst, ed., Proc. SPIE **3377**, 106–113 (1998).
8. J. G. Harris and Y.-M. Chiang, "Nonuniformity correction of infrared image sequences using the constant-statistics constraint," IEEE Trans. Image Process. **8**, 1148–1151 (1999).
9. Y.-M. Chiang and J. G. Harris, "An analog integrated circuit for continuous-time gain and offset calibration of sensor arrays," J. Analog Int. Circuits Signal Process. **12**, 231–238 (1997).
10. W. F. O'Neil, "Experimental verification of dithered scan non-uniformity correction," in *Proceedings of the 1996 International Meeting of the Infrared Information Symposium Specialty Group on Passive Sensors* (Infrared Information Analysis Center, Ann Arbor, Michigan, 1997), Vol. 1, pp. 329–339.
11. R. C. Hardie, M. M. Hayat, E. E. Armstrong, and B. Yasuda, "Scene based nonuniformity correction using video sequences and registration," Appl. Opt. **39**, 1241–1250 (2000).
12. B. M. Ratliff, M. M. Hayat, and R. C. Hardie, "An algebraic algorithm for nonuniformity correction in focal-plane arrays," J. Opt. Soc. Am. A **19**, 1737–1747 (2002).
13. K. C. Hepfer, S. R. Horman, and B. Horsch, "Method and device for improved IR detection with compensations for individual detector response," U.S. patent 5,276,319 (4 January 1994).
14. M. M. Hayat, S. Torres, E. E. Armstrong, B. Yasuda, and S. C. Cain, "Statistical algorithm for non-uniformity correction in focal plane arrays," Appl. Opt. **38**, 772–780 (1999).
15. E. E. Armstrong, M. M. Hayat, R. C. Hardie, S. N. Torres, and B. Yasuda, "Nonuniformity correction for improved registration and high resolution image reconstruction in IR imagery," in *Applications of Digital Image Processing XXII*, A. G. Tescher, ed., Proc. SPIE **3808**, 150–161 (1999).
16. S. N. Torres, M. M. Hayat, E. E. Armstrong, and B. Yasuda, "A Kalman-filtering approach for nonuniformity correction in focal-plane array sensors," in *Infrared Imaging Systems: Design, Analysis, Modeling, and Testing XI*, G. C. Hulst, ed., Proc. SPIE **4030**, 196–205 (2000).
17. S. N. Torres and M. M. Hayat, "Kalman filtering for adaptive nonuniformity correction in infrared focal plane arrays," J. Opt. Soc. Am. A **20**, 470–480 (2003).
18. G. Minkler and J. Minkler, *Theory and Applications of Kalman Filtering* (Magellan, Palm Bay, Fla., 1993).
19. C. Therrien, *Discrete Random Signals and Statistical Signal Processing* (Prentice-Hall, Englewood Cliffs, N.J., 1992).
20. S. N. Torres, "A Kalman filtering approach for non-uniformity correction in infrared focal plane array sensors," Ph.D. dissertation (University of Dayton, Ohio, 2001).
21. M. Schultz and L. Caldwell, "Nonuniformity correction and correctability of infrared focal plane arrays," in *Infrared Imaging Systems: Design, Analysis, Modeling, and Testing VI*, G. C. Hulst, ed. Proc. SPIE **2470**, 200–211 (1995).
22. Z. Wang and A. Bovik, "A universal image quality index," IEEE Signal Process. Lett. **9**, 81–84 (2002).
23. J. L. Hennessy and D. A. Patterson, *Computer Organization and Design: The Hardware/Software Interface* (Morgan Kaufmann, Los Altos, Calif., 1997).